

Rubidium in Barium stars

M. P. Roriz^{1b},¹★ M. Lugaro,^{2,3,4}★ C. B. Pereira,¹★ N. A. Drake^{1b},^{5,6} S. Junqueira¹ and C. Sneden⁷

¹Observatório Nacional/MCTI, Rua Gen. José Cristino, 77, 20921-400, Rio de Janeiro, Brazil

²Konkoly Observatory, Research Centre for Astronomy and Earth Sciences, Konkoly Thege Miklós út 15-17, H-1121 Budapest, Hungary

³ELTE Eötvös Loránd University, Institute of Physics, Budapest 1117, Pázmány Péter sétány 1/A, Hungary

⁴School of Physics and Astronomy, Monash University, VIC 3800, Australia

⁵Laboratory of Observational Astrophysics, Saint Petersburg State University, Universitetski pr. 28, 198504, Saint Petersburg, Russia

⁶Laboratório Nacional de Astrofísica/MCTI, Rua dos Estados Unidos 154, Bairro das Nações, 37504-364, Itajubá, Brazil

⁷Department of Astronomy and McDonald Observatory, The University of Texas, Austin, TX 78712, USA

Accepted 2020 December 9. Received 2020 December 8; in original form 2020 October 1

ABSTRACT

Barium (Ba) stars are chemically peculiar stars that display in their atmospheres signatures of the *slow* neutron-capture (*s*-process) mechanism that operates within asymptotic giant branch (AGB) stars, an important contributor to the cosmic abundance. The observed chemical peculiarity in these objects is not due to self-enrichment, but to mass transfer between the components of a binary system. The atmospheres of Ba stars are therefore excellent astrophysical laboratories, providing strong constraints for the nucleosynthesis of the *s*-process in AGB stars. In particular, rubidium (Rb) is a key element for the *s*-process diagnostic because it is sensitive to the neutron density and hence its abundance points to the main neutron source of the *s*-process in AGB stars. We present Rb abundances for a large sample of 180 Ba stars from high-resolution spectra ($R = 48\,000$), and we compare the observed [Rb/Zr] ratios with theoretical predictions from *s*-process models in AGB stars. The target Ba stars in this study display [Rb/Zr] < 0, showing that Rb was not efficiently produced by the activation of the branching points at ^{85}Kr and ^{86}Rb . Model predictions from the Monash and FRUITY datasets of low-mass ($\lesssim 4\,M_{\odot}$) AGB stars are able to cover the Rb abundances observed in the program Ba stars. These observations indicate that the $^{13}\text{C}(\alpha, n)^{16}\text{O}$ reaction is the main neutron source of the *s*-process in the low-mass AGB companions of the observed Ba stars. We have not found in the present study candidate companions for former IR/OH massive AGB stars.

Key words: nuclear reactions, nucleosynthesis, abundances – stars: abundances – stars: chemically peculiar.

1 INTRODUCTION

Barium (Ba) stars are chemically peculiar stars first identified by Bidelman & Keenan (1951). These objects provide an excellent opportunity to investigate more closely the neutron-capture nucleosynthesis mechanisms of the elements heavier than iron. This is because Ba stars are G/K spectral-type giants or dwarfs exhibiting strong atomic lines of the heavy elements, in particular, Ba II and Sr II lines, as well as CH, CN, and C₂ molecular band features.

The elements heavier than iron present in the Universe are created mostly by the *slow* neutron-capture (*s*-process; Käppeler et al. 2011) and *rapid* neutron-capture (*r*-process; Cowan et al. 2019) mechanisms. The *s*-process, producing roughly half of the cosmic abundance of the elements from Sr to Pb, takes place within asymptotic giant branch (AGB; Herwig 2005) stars during their thermally-pulsing phase. Neutron-captures on pre-existing iron nuclei, which act as seeds, are followed by β decays, creating new elements. Low- and intermediate-mass (1–8 M_{\odot}) AGB stars have an inert C/O core surrounded by an extensive H-rich convective envelope. Between the inert core and the base of the convective envelope, there is a thin region where two layers burn hydrogen (H-

shell burning) and helium (He-shell burning) alternately. Most of the time, the H-shell burning is active (during the so-called ‘interpulse periods’) being interrupted by brief and recurring episodes of He-shell burning (the thermal pulses; TP). The *s*-process takes place in the thin He-rich region between the two layers burning H and He. After each TP, the processed material is brought to the stellar surface by a mixing mechanism usually referred to as third dredge-up (TDU). The free neutrons that drive the *s*-process come from two possible sources: the $^{13}\text{C}(\alpha, n)^{16}\text{O}$ and the $^{22}\text{Ne}(\alpha, n)^{25}\text{Mg}$ reactions (Straniero et al. 1997; Gallino et al. 1998; Goriely & Mowlavi 2000; Busso et al. 2001; Lugaro et al. 2003; Karakas & Lattanzio 2014). For low-mass ($\lesssim 3\,M_{\odot}$) AGB stars, the $^{13}\text{C}(\alpha, n)^{16}\text{O}$ reaction is the main neutron source and it is activated during the interpulse periods, at temperatures $T \sim 10^8$ K, releasing a neutron density $N_n \sim 10^7\text{ cm}^{-3}$ under radiative conditions. The $^{22}\text{Ne}(\alpha, n)^{25}\text{Mg}$ reaction is mainly activated in intermediate-mass (4–8 M_{\odot}) AGB stars during the thermal pulses, at higher temperatures $T \gtrsim 3 \times 10^8$ K, under convective conditions, providing neutron densities up to $N_n \sim 10^{12}\text{ cm}^{-3}$.

However, Ba stars are not yet evolved to the AGB phase and therefore they could not have produced the heavy element enhancements observed in their atmospheres. In fact, these elements were created within a more massive and evolved binary companion (now an undetectable white dwarf) when it passed through the AGB phase, and the *s*-rich material was transferred to the less evolved component

* E-mail: michelle@on.br (MPR); maria.lugaro@csfk.mta.hu (ML); claudio@on.br (CBP)

(now observed as a Ba star) through stellar winds that contaminated its atmosphere. Indeed, observations of radial velocities made several decades ago (McClure, Fletcher & Nemec 1980; McClure 1983; McClure & Woodworth 1990) confirmed that Ba stars belong to binary systems so that the chemical peculiarities in these objects can be explained by the mass transfer scenario. More recent studies of the binarity of Ba stars have been reported, for example, by Jorissen et al. (2019) and Escorza et al. (2019).

The chemical abundance pattern displayed in the atmospheres of the Ba stars is therefore a record of the nucleosynthesis process of the AGB companion stars and can serve as a useful tool to be compared to theoretical predictions from *s*-process models provided, for example, by FRUITY¹ (Cristallo et al. 2009, 2011, 2015), Monash (Fishlock et al. 2014; Karakas & Lugaro 2016; Karakas et al. 2018), NuGrid collaboration (Battino et al. 2016, 2019; Pignatari et al. 2016), and SNUPPAT models (Yagüe López et al., in preparation). These abundances provide important diagnostics for the neutron exposure, neutron density, and temperature of the *s*-process environments. Ba stars have the advantage to be warmer (4000–6000 K) than AGB stars (3000–4000 K) and hence their spectra are easier to be studied than those of AGB stars.

Detailed chemical abundances in Ba stars have been presented by several authors (e.g. Smith 1984; Allen & Barbuy 2006a, b; Smiljanic, Porto de Mello & da Silva 2007; Pereira et al. 2011; de Castro et al. 2016; Karinkuzhi et al. 2018a, b); in particular, de Castro et al. (2016) provided an internally consistent analysis of 182 Ba stars and candidates, the largest single sample to date. These authors determined for the whole sample the atmospheric parameters and the $[X/Fe]^2$ ratios for light (ls) and heavy (hs) *s*-process elements belonging to the first (Y and Zr) and second (La, Ce, and Nd) *s*-process peaks, respectively. Later, Cseh et al. (2018) compared the $[Ce/Y]$, $[Ce/Zr]$, $[Nd/Y]$, and $[Nd/Zr]$ ratios derived by de Castro et al. (2016) to theoretical predictions from *s*-process models. That study found a good agreement with the models, confirming the ¹³C as main neutrons source in low-mass AGB stars (see fig. 6 of Cseh et al. 2018) and that the stellar metallicity plays a major role in shaping the observed abundance patterns.

However, abundances of other heavy elements are necessary to provide more constraints with respect to operation of the *s*-process in AGB stars. In particular, the production of rubidium (Rb) increases significantly if the ²²Ne neutron source is activated during the TPs, thanks to branches along the *s*-process path (e.g. Lugaro & Chieffi 2011; van Raai et al. 2012). Being sensitive to neutron density, Rb can tell us about the neutron source in AGB stars and has been the subject of many studies. In fact, Rb has been studied in AGB stars of our Galaxy (Abia et al. 2001; García-Hernández et al. 2006, 2007; van Raai et al. 2012; Pérez-Mesa et al. 2017) and the Magellanic Clouds (García-Hernández et al. 2009), in globular clusters (D’Orazi et al. 2013), open clusters (Reddy, Giridhar & Lambert 2013), disc stars (Tomkin & Lambert 1999), and M, MS, and S stars (Lambert et al. 1995). For Ba stars, the earlier work of Smith & Lambert (1984) reported the analysis of Rb and Nb in ζ Capricorni, a prototype Ba star; Tomkin & Lambert (1983) also studied Rb and other heavy elements in the Ba star HR 774; Tomkin & Lambert (1986) analyzed

Rb in more 2 Ba stars. Malaney (1987) presented an analysis of *s*-process abundances, including Rb, for 3 Ba stars previously studied in the literature; Malaney & Lambert (1988) studied a sample of 9 Ba stars, of which 2 objects had their Rb abundance determined. Abia & Wallerstein (1998) added 2 Ba stars to their sample of SC and S stars and presented results for Rb. More recently, Karinkuzhi et al. (2018b) analyzed a sample of 18 Ba stars, with Rb abundances calculated for 10 objects. Measuring Rb in a large sample of Ba stars offers us an excellent opportunity to investigate the *s*-process mechanism in AGB stars.

We have determined Rb abundances for a sample of 180 Ba stars, greatly extending and improving the available data for Rb in these objects, and have used the results to study the *s*-process mechanism in AGB stars. In Section 2, we explain the role played by Rb on the *s*-process path; in Section 3, we present the target stars, selected from sources in the literature. In Section 4, we describe our procedure to take account the hyperfine structure (hfs) effects and the isotopic ratio of Rb; in Section 5, we present the methodology adopted in this study and then we discuss the new results for Rb abundances for the program Ba stars in Section 6. We compare the results with recent theoretical predictions of the *s*-process models in Section 7. In Section 8, we highlight our conclusions.

2 RB AS A NEUTRON DENSITY MONITOR

It is well known that both the *s*-process and the *r*-process contribute to the synthesis of Rb in the Universe. As noted by van Raai et al. (2012), the contribution fraction due to the *s*-component can vary widely, depending on the adopted *s*-process model. For example, Sneden et al. (1996, their table 5) reported 97 per cent for the *s*-process contribution, whereas Arlandini et al. (1999, their table 2) presented the values of 22 per cent and 59 per cent, respectively for the AGB star and classical models. Burris et al. (2000, their table 5) and Travaglio et al. (2004, their table 3) estimated approximately 50 per cent for the *s*-processes contribution to the synthesis of Rb. Understanding the fractional contribution of the *s*-process to the Rb production is crucial to constraint the *r*-process component and its sources in the Galaxy.

The abundance of Rb depends on the two unstable nuclei: ⁸⁵Kr (with half-life $t_{1/2} = 11$ years) and ⁸⁶Rb ($t_{1/2} = 19$ days), which act as branching points along the *s*-process path. These isotopes can capture a neutron or suffer a β decay, depending on the relative probabilities of the two channels. The selected channel depends on the available neutron density at the *s*-process site. The isotope ⁸⁵Kr can decay to the stable ⁸⁵Rb or it can capture a neutron, branching the *s*-process path to ⁸⁶Kr (we refer the reader to the fig. 1 of van Raai et al. 2012); after other neutron-capture, ⁸⁷Kr readily decays to the long-lived ⁸⁷Rb. This isotope has a half-life $t_{1/2} > 10^{10}$ years and therefore it can be considered as stable. Similarly, ⁸⁶Rb can decay into ⁸⁶Sr or capture a neutron to produce directly ⁸⁷Rb. If the neutron density is high ($N_n > 10^8 \text{ cm}^{-3}$), the branching points in ⁸⁵Kr and ⁸⁶Rb are open, favouring the production of ⁸⁷Rb. Because ⁸⁷Rb has a magic number of neutrons ($N = 50$), it has a small neutron-capture cross-section ($\sigma_{87} = 15.7 \text{ mbarn}$ at 30 keV)³ and as a consequence it tends to accumulate, resulting in an increase in the overall amount of Rb.⁴ Therefore, the isotopes ⁸⁵Rb and ⁸⁷Rb are very sensitive to

¹FRUIT-Repository of Updated Isotopic Tables & Yields; available at <http://fruity.oa-teramo.inaf.it/>

²In this work, we have used the standard spectroscopy notation for the abundance ratio between two generic elements, A and B: $[A/B] = \log(n_A/n_B) - \log(n_A/n_B)_\odot$ and $\log \epsilon(A) = \log(n_A/n_H) + 12$, where n denotes the elemental abundance by number and the \odot symbol refers to the solar values.

³KADONIS database (Dillmann et al. 2006) online at <https://www.kadonis.org>
⁴Note that because also ⁸⁶Kr has a magic number of neutrons, its production via the activation of the ⁸⁵Kr branching point may actually decrease the final Rb abundance, see details in van Raai et al. (2012).

the neutron density. Unfortunately, it is not possible to evaluate the isotopic ratio $^{85}\text{Rb}/^{87}\text{Rb}$ directly from spectra because the isotopic splitting is small compared to typical spectral line breadths; see Section 4 for details.

Fortunately, the ratio between Rb and its neighbors, for example [Rb/Sr] or [Rb/Zr], can be used for the same purpose. From theoretical predictions of the *s*-process models, the [Rb/Zr] ratio has a positive value if the main neutron source is the $^{22}\text{Ne}(\alpha, n)^{25}\text{Mg}$ reaction, whereas [Rb/Zr] has a negative value if the main neutron source is the $^{13}\text{C}(\alpha, n)^{16}\text{O}$ reaction. Lambert et al. (1995) used the [Rb/Sr] ratio to demonstrate that the $^{13}\text{C}(\alpha, n)^{16}\text{O}$ reaction is main neutron source in M, MS, and S stars and Abia et al. (2001) also used the abundance between Rb and its neighbors, Sr, Y, and Zr, to show that C stars must be low-mass AGB stars. Instead, García-Hernández et al. (2006) found [Rb/Zr] > 0 in Galactic intermediate-mass AGB stars and similarly, for intermediate-mass AGB stars in the Magellanic Clouds, García-Hernández et al. (2009) obtained [Rb/Zr] > 0. These positive ratios were interpreted as the results of the *s*-process driven by the $^{22}\text{Ne}(\alpha, n)^{25}\text{Mg}$ reaction inside these intermediate-mass AGB stars.

3 SAMPLE STARS

The objects analyzed in this study were selected from the previous work of de Castro et al. (2016). We also included in the present analysis 11 metal-rich ([Fe/H] $\geq +0.1$) Ba stars, analyzed by Pereira et al. (2011), 2 Ba stars of the open cluster NGC 5822 (Katime Santrich, Pereira & de Castro 2013), and the star HD 10613, studied by Pereira & Drake (2009). The final sample, therefore, consists of 180 objects with metallicities, [Fe/H], ranging from -1.0 to $+0.30$ dex and effective temperatures, T_{eff} , in the interval of 4000 to 5500 K. In all the above-mentioned studies, we adopted the model atmospheres provided by Kurucz (1993). The mass distribution of the sample has a peak around $2.5 M_{\odot}$ (see de Castro et al. 2016, and their fig. 10). For nearly all stars added from other papers, we adopted their recommended model atmospheric parameters. However, we determined new atmospheric parameters for HD 10613 in order to improve the difference between the metallicity of the model and the final iron abundance, from 0.3 dex in the previous analysis (Pereira & Drake 2009) to 0.05 dex, in the present work. We have obtained for this star the following atmospheric parameters: $T_{\text{eff}} = 4950$ K, $\log g = 2.7$ dex, $\xi = 1.0$ km s $^{-1}$ and [Fe/H] = -0.92 dex.

The previous papers contributing to our Rb study used high-resolution spectra in the optical region obtained with the Fiber-fed Extended Range Optical Spectrograph (FEROS; Kaufer et al. 1999) at the 1.52 and 2.2 m ESO telescopes at La Silla (Chile), between the years 1999 and 2010. FEROS has a resolving power $R = \lambda/\Delta\lambda = 48\,000$ covering the spectral region between 3800 Å and 9200 Å.

4 HYPERFINE STRUCTURE

The energy levels of Rb are strongly affected by hfs effects due to coupling between the total electron angular momentum, **J**, and the total nuclear angular momentum, **I**. As a consequence of this interaction between **I** and **J**, the atomic terms are splitted into components with typical energy separation orders of magnitude smaller than the fine-structure levels. Each one of these hyperfine levels is labelled by the quantum number *F*, associated with the total atomic angular momentum, **F** = **I** + **J**, that assumes only specific values, namely:

$$F = I + J, I + J - 1, I + J - 2, \dots, |I - J|, \quad (1)$$

Table 1. The *A* and *B* hyperfine constants adopted in this work.

	Lower level		Upper level		
	<i>A</i> (MHz)	Ref.	<i>A</i> (MHz)	<i>B</i> (MHz)	Ref.
^{85}Rb	1011.911	1	25.009	25.039	2
^{87}Rb	3417.341	3	84.718	12.497	4

Notes. References: (1) Nez et al. (1993); (2) Rapol, Krishna & Natarajan (2003); (3) Bize et al. (1999); (4) Ye et al. (1996).

where *I* and *J* are the quantum numbers associated with **I** and **J**, respectively. Hyperfine transitions are those involving the quantum number *F* and they are also governed by the selection rules, $\Delta F = 0, \pm 1$, but the $0 \rightarrow 0$ transitions are not allowed.

The energy shift, ΔE , of a hyperfine component from the ‘center of gravity’ of the line is given by the Casimir formula, presented in the textbook of Woodgate (1983):

$$\Delta E = \frac{AK}{2} + \frac{B}{8} \frac{3K(K+1) - 4I(I+1)J(J+1)}{I(2I-1)J(2J-1)}, \quad (2)$$

where *A* and *B* are the hfs constants of magnetic dipole and electric quadrupole, respectively, and *K* is defined as:

$$K = F(F+1) - I(I+1) - J(J+1). \quad (3)$$

From equation (2), we are able to obtain the hfs spectrum for a given isotope, as long as the hfs constants, *A* and *B*, and the quantum numbers *I* and *J* involved are known. We applied the equation (2) in order to derive the hyperfine components for the two Rb isotopes, as described below.

4.1 Hyperfine structure of Rb

Rb is naturally present in the form of the isotopes ^{85}Rb and ^{87}Rb , with relative abundances of 72.2 per cent and 27.8 per cent, respectively, in the Solar System. In addition, each of these isotopes has a different nuclear spin quantum number: ^{85}Rb has $I_{85} = 5/2$, whereas ^{87}Rb has $I_{85} = 3/2$. To determine Rb abundance in the sample of Ba stars we have considered the Rb I D_2 resonance line at 7800.2 Å.⁵ This line is due to the $5^2S_{1/2} - 5^2P_{3/2}$ transition between the fine-structure doublet, separated by 12 816.545 cm $^{-1}$. A summary of the levels and hfs constants for Rb and other species is provided, for example, by Morton (2000), Sansonetti (2006), and Grevesse et al. (2015). As mentioned above, the magnetic interaction between nuclear spin angular momentum and electronic angular momentum gives rise to hyperfine splits in the fine-structure terms and as a consequence, six hyperfine transitions for each Rb isotope are raised under the selection rules. From equation (2), we then calculated the wavelengths due to transitions between the hyperfine levels, $F_l - F_u$, of the ^{85}Rb and ^{87}Rb isotopes. In Table 1, we show the adopted *A* and *B* hfs constants and their respective sources. For the ground state ($J_l = 1/2$) of the Rb I D_2 line, the second term in equation (2) is not applied, only the first one.

The relative weights of the hyperfine transitions can be obtained from values tabulated by White & Eliason (1933). According to

⁵The 7800.2 Å line is one member of the Rb I ground-state resonance doublet and its multiplet companion lies at 7947.6 Å, which is detectable in giant stars with very large Rb abundances. However, its transition probability is half that of the 7800.2 Å line, creating a weak absorption even in our Ba stars. Additionally, the 7947.6 Å line is severely blended with a CN feature, rendering it of little use for abundance studies. The 7947.6 Å line will not be considered further in this paper.

Table 2. Hyperfine structure components of Rb I D_2 line at 7800.2 Å. We also provided in the last column the log gf values taking in account the isotopic ratio for Rb adopted in this work.

λ (Å)	log gf	
^{85}Rb	No isotopic ratio	$^{85}\text{Rb}/^{87}\text{Rb} = 2.59$
7800.233	−0.750	−0.891
7800.234	−0.653	−0.795
7800.235	−0.766	−0.908
7800.292	−0.289	−0.430
7800.294	−0.653	−0.795
7800.296	−1.199	−1.340
^{87}Rb		
7800.183	−0.669	−1.225
7800.187	−0.669	−1.225
7800.188	−1.067	−1.623
7800.316	−0.222	−0.778
7800.322	−0.669	−1.225
7800.325	−1.371	−1.927

these intensities, it is possible to determine the log gf value for each hyperfine transition by distributing the total log gf of the Rb I D_2 line. For this transition, we have adopted log $gf = 0.137$, provided by VALD⁶ database (Piskunov et al. 1995; Ryabchikova et al. 2015). In Table 2, we show the hyperfine components and their respective log gf values for the two Rb isotopes derived in this work. In the following section, we use these results to obtain the Rb abundances.

5 METHODOLOGY

Abundances were determined by comparing observed and synthetic spectra. To compute the synthetic spectra, we used the current version of the local thermodynamic equilibrium (LTE) plane-parallel line analysis code MOOG⁷ (Snedden 1973). The best fit between observed and synthetic spectra provides the final Rb abundance. Our synthetic spectrum line list was constructed from the VALD database that includes the CN transitions and atomic lines of Si I and Mg I close to 7800.2 Å region. In Fig. 1 we show the observed and synthetic spectra in the spectral region between 7799 and 7802 Å for four stars of our sample, where we identify the contributions of the atomic and molecular lines; as the Fig. 1 shows, the Rb I line is partially blended with the Si I line. For each star, we run the synthesis for three different values of the log $\epsilon(\text{Rb})$ abundance. We adopted the solar Rb abundance, log $\epsilon(\text{Rb}) = 2.60 \pm 0.15$, as recommended by Grevesse & Sauval (1998). The same value is also recommended by Asplund, Grevesse & Sauval (2005) and Lodders, Palme & Gail (2009), while a slightly smaller value is reported by Asplund et al. (2009), i.e. 2.52 ± 0.10 and Grevesse et al. (2015), i.e. 2.47 ± 0.07 . To make the synthetic spectra, we assumed the Solar System isotopic ratio, $^{85}\text{Rb}/^{87}\text{Rb} = 2.59$, since this ratio cannot be measured directly from the spectra, as we previously discussed in Section 2. Abia & Wallerstein (1998) and Abia et al. (2001), for example, argued that although this ratio varies depending on the neutron density where the s -process is taking place, the final Rb abundance does not show significant variations. Indeed, we tested synthetic spectra for different isotopic ratios and we did not notice changes in the final Rb abundance.

⁶ Available at <http://vald.astro.uu.se>

⁷ Available at <https://www.as.utexas.edu/~chris/moog.html>

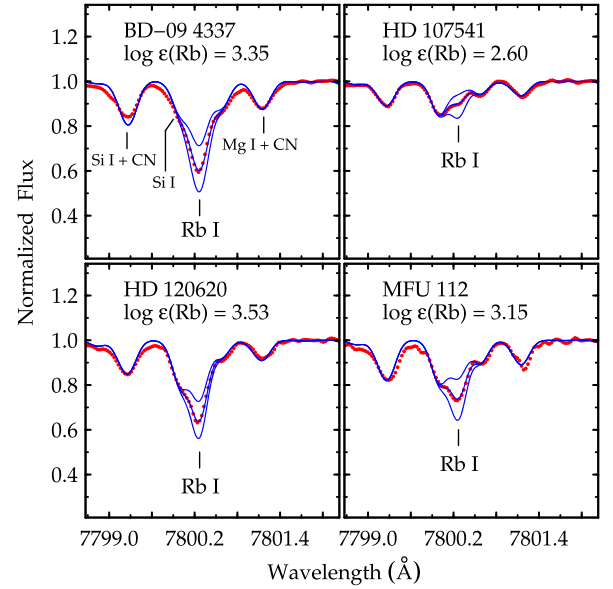


Figure 1. Region close to the Rb I D_2 line at 7800.2 Å, where we show the observed (red points) and synthetic (blue lines) spectra for four objects belonging to our programme stars. In each panel, the best fit provides the final Rb abundance, labeled on the top of panels; the lower and upper blue lines are the synthetic spectra for $\Delta \log \epsilon(\text{Rb}) = \pm 0.3$ dex around the best fit.

5.1 Abundances and uncertainties

The final Rb abundances for the programme stars are presented in Table A1. We show in Columns 4 and 5 the Rb abundances by number, log $\epsilon(\text{Rb})$, and the [Rb/Fe] ratios. Column 9 gives the computed [Rb/Zr] ratios. The uncertainties in the abundance ratios coming from two different sources: the errors in the parameters of stellar models (σ_{atm}) and the dispersion of the observed abundance (σ_{lin}) due to the number of lines used to derive it.

In order to take account the error bars in the [Rb/Zr] ratios, we adopted the same steps described by Cseh et al. (2018, see their section 2 for more details) who combined these two sources of uncertainties in their study. We first separated the target stars into three groups according to the temperatures ranges: group 1 (5000–5400 K), group 2 (4700–4950 K), and group 3 (4100–4600 K), based on the tables 9, 10, and 11 of de Castro et al. (2016), respectively, where each group is represented by a typical star. For these representative stars, we vary the atmospheric parameters (T_{eff} , log g , ξ , [Fe/H]) and then we compute the corresponding variation in the logarithmic Rb abundance. The uncertainty for the [Rb/Zr] ratio, coming from the stellar parameters, was calculated according to the following equation:

$$\sigma_{\text{atm}}^2 = \left(\frac{\partial [\text{Rb/Zr}]}{\partial T_{\text{eff}}} \right)^2 + \left(\frac{\partial [\text{Rb/Zr}]}{\partial \log g} \right)^2 + \left(\frac{\partial [\text{Rb/Zr}]}{\partial \xi} \right)^2 + \left(\frac{\partial [\text{Rb/Zr}]}{\partial [\text{Fe/H}]} \right)^2 + \left(\frac{\partial [\text{Rb/Zr}]}{\partial W_{\lambda}} \right)^2. \quad (4)$$

The last term in equation (4), however, was applied only for Zr, taking account variations in the Zr abundance due to changes in the equivalent width, W_{λ} .

We then calculated the uncertainties coming from the dispersion of the observed abundance for each object of the sample. This step was applied only for Zr, when three or more lines were available. For Rb, however, we were not able to calculate its uncertainties coming

from dispersion of the lines once we have only one available line for this element. In this way,

$$\sigma_{\text{lin}}^2 = \left(\frac{\sigma_{\text{obs}}}{\sqrt{N}} \right)_{\text{Zr}}^2, \quad (5)$$

where σ_{obs} is the dispersion of the abundances among different lines and N is the number of lines used to derive the respective abundance.

Finally, we computed the final uncertainties of the [Rb/Zr] ratios by taking the root square of the sum of the square of the uncertainties derived from the step 1 and step 2:

$$\sigma_{[\text{Rb/Zr}]}^2 = \sigma_{\text{atm}}^2 + \sigma_{\text{lin}}^2. \quad (6)$$

The final values for $\sigma_{[\text{Rb/Zr}]}$ are shown in the Column 10 of the Table A1.

6 DISCUSSION

The data from Table A1 are plotted in Fig. 2, together with the sample of 10 Ba stars analyzed by Karinkuzhi et al. (2018b). In panels (a) and (b) of the Fig. 2, we plot [Rb/Fe] against [Fe/H] and [Zr/Fe], respectively. The correlation between the Rb and Zr abundances in panel (b) and the relatively small scatter indicates that higher Rb abundances are not due to a more efficient activation of the branching points in the stars where they are observed, but that they are due to a generally more efficient *s*-process (i.e. overall higher *s*-process abundances in the intershell) and/or more efficient mixing of the *s*-process material into the envelope via the TDU, and/or a more efficient mass transfer from the AGB on to the Ba star. As expected, the three most Rb-rich stars of the whole sample are also among the most Zr-rich stars (HD 120620 with [Rb/Fe] = 1.07 and [Zr/Fe] = 1.26, BD -09°4337 with [Rb/Fe] = 0.99 and [Zr/Fe] = 1.51 and MFU 112 with [Rb/Fe] = 0.98 and [Zr/Fe] = 1.26); we also show the observed and synthetic spectra of these objects in the Fig. 1. Higher *s*-process and mixing efficiencies are usually achieved at lower metallicities, in agreement with the general trend shown in panel (a).

We compare the behaviour of [Rb/Zr] against [Rb/Fe] and [Zr/Fe] in panels (c) and (d), respectively, of the Fig. 2. These two panels demonstrate that the variations of roughly an order of magnitude observed in [Rb/Zr] are predominantly due to corresponding variations in Zr, rather than in Rb. In fact, the data in panel (c) do not show a trend, in contrast with panel (d), where there is an anti-correlation between [Rb/Zr] and [Zr/Fe]. Only the three stars with the highest [Rb/Fe] ratios already noted above are significantly outside the scatter area. In any case all the plotted stars display [Rb/Zr] < 0, indicating low neutron density when the *s*-process took place inside the AGB companion. We will discuss this in the light of the nucleosynthesis models in the Section 7, where we compare the Rb abundances with theoretical predictions.

This paper has concentrated only on light *s*-process elements Rb and Zr. The previous works of de Castro et al. (2016), Pereira et al. (2011), Katime Santrich et al. (2013), and Pereira & Drake (2009) published abundances of several elements (Na, Al, α -elements and iron group) and *s*-process elements (Y, La, Ce, and Nd) in addition to Zr used in this paper. From these papers and many others in the literature some general conclusions are already understood: (a) the tight correlation between Y and Zr abundances; (b) the larger overabundances of heavy *s*-process elements La, Ce, Nd with respect to the lighter ones Y and Zr (see also interpretation in Cseh et al. 2018); and (c) the lack of any obvious correlation between the α - and Fe-group abundances and those of the *s*-process.

We are conducting an abundance analysis of more elements in the program stars. The papers mentioned above limited their investigation to equivalent width analyses of lines assumed to be single features. For Ba stars, however, this is inadequate for lanthanum (hs), for example, due to hyperfine and isotopic transition splitting and often heavy feature contamination by other species. Therefore, we are undertaking a re-examination of the previous results for this element as well as a significant extension to include at least the following elements: Sr, Nb, Mo, and Ru (ls) and Sm and Eu (usually *r*-process). These new abundances, based on equivalent width analyses (Sr, Mo, Ru, and Sm) and on synthetic spectrum computations (Nb, La, and Eu), will be reported by Roriz et al. (in preparation).

6.1 Particular objects

As we have mentioned, the stars HD 120620, BD -09°4337, and MFU 112 show Rb abundances comparatively higher than the other stars belonging to our sample and therefore these objects deserve additional comments. In this sense, we have examined the position of these three star in two plots in Fig. 3: [Rb/Fe] versus [hs/ls] (panel a) and [Rb/Fe] versus [s/Fe] (panel b), where [hs/ls] = [hs/Fe] - [ls/Fe], being [hs/Fe] and [ls/Fe] respectively the mean abundance of the heavy (Ce and Nd) and light (Y and Zr) *s*-process elements, and [s/Fe] is the mean abundance of the *s*-elements (Y, Zr, Ce, and Nd). In this study, we are not considering lanthanum in the evaluation of the [hs/ls] and [s/Fe] indexes, since the abundance of this element is strongly affected by hyperfine structure interaction, as we pointed out in the previous paragraph. The [hs/ls] index is commonly used as an indicator of the *s*-process efficiency. The target Ba stars in this study show [hs/ls] ranging from -0.4 to 0.7 dex; the stars HD 120620 ([hs/ls]=0.26; [s/Fe]=1.42), BD -09°4337 ([hs/ls]=0.19; [s/Fe]=1.40), and MFU 112 ([hs/ls]=0.38; [s/Fe] = 1.31) have a normal [hs/ls] ratio compared to the other stars in the present sample.

7 COMPARISON TO NUCLEOSYNTHESIS MODELS

In Fig. 4 we compare the [Rb/Zr] ratio as function of metallicity to four different sets of available models of the *s*-process in AGB stars of different masses and metallicities, corresponding to those of the observed Ba stars. These models can satisfy the minimal requirement of reaching the upper values of the observed [Rb/Fe] range, see panel (a) of Fig. 2. However, the comparison between models and data obtained in this work for [Rb/Fe] is only indicative because binary mass transfer will necessarily lower the predicted values. To reach robust conclusions on such comparison a detailed analysis of binary interaction is required, which is beyond the scope of the present work. Here, we focus on the nucleosynthesis and therefore on the intrinsic [Rb/Zr] ratio. This ratio is affected more by the neutron source than by the binary interaction because both elements are expected to be diluted by roughly the same factor.

As discussed at length previously (Abia et al. 2001; van Raai et al. 2012), the stellar mass plays the most significant role in the activation of the ^{22}Ne neutron source and the final [Rb/Zr] ratios. AGB stars of higher masses are generally hotter, so that this neutron source is more efficiently activated, generating higher neutron densities and therefore higher [Rb/Zr] ratios are predicted. While this effect presents a non-linear and model-dependent metallicity dependence, it is in general verified for the Monash and the FRUITY models. Both Monash and FRUITY models of low-mass (1.5 M_{\odot}) and high metallicity experience some ingestion of ^{13}C nuclei from the ^{13}C pocket into the following TP. This raises the neutron density of the

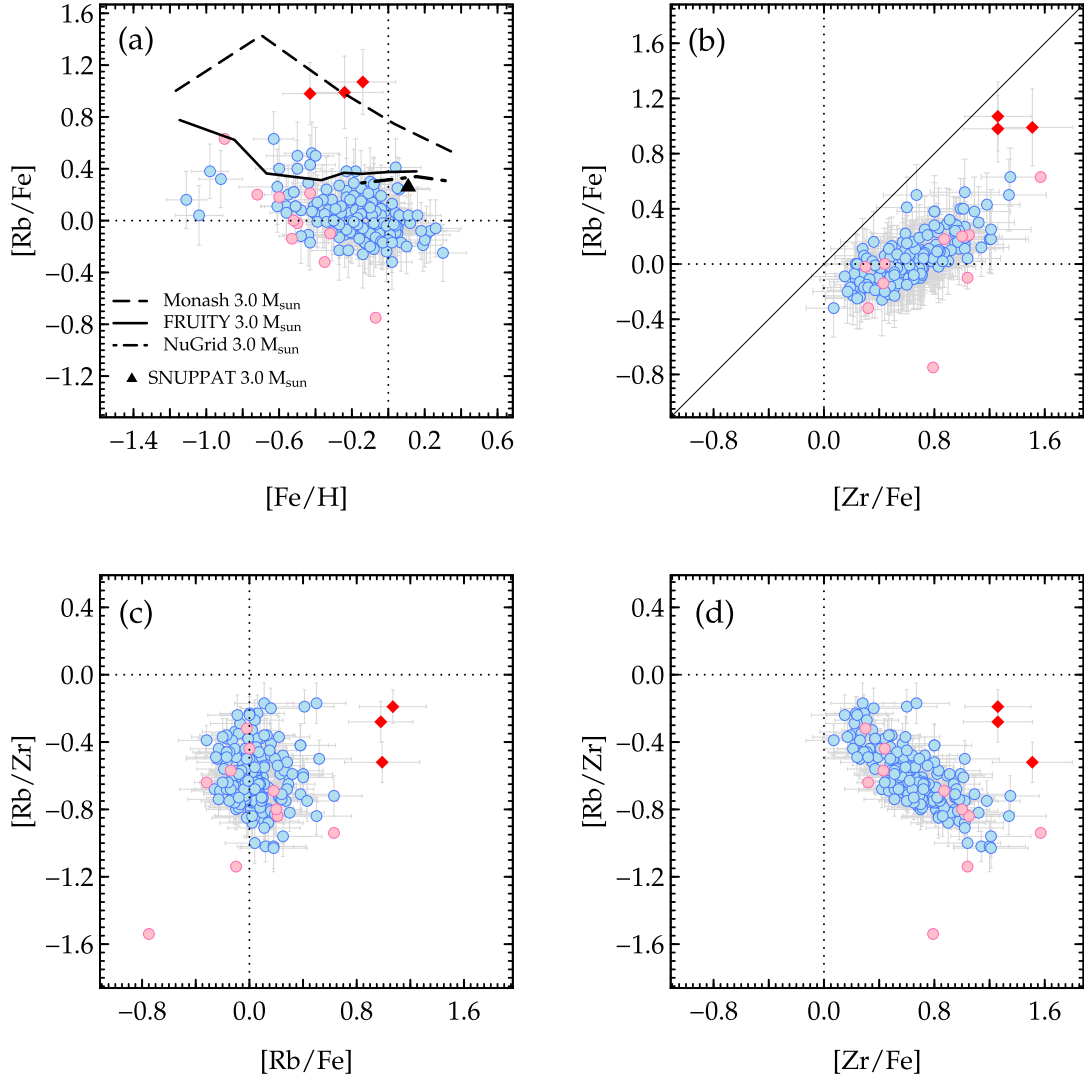


Figure 2. Different abundance ratios for the Ba stars (blue dots) studied in this work. The [Zr/Fe] and [Fe/H] ratios were taken from de Castro et al. (2016). We have added in the plots (magenta dots) the sample stars previously analyzed by Karinkuzhi et al. (2018b). We indicate the three more Rb-rich stars in red diamonds on the panels. In panel (a) we also plot a selection (the 3 M_⊙) of the AGB model predictions we consider in Fig. 4 for the comparison to the [Rb/Zr] ratio. We also plot them here to show that these models can reach the upper values of the observed [Rb/Fe] range. This is a necessary but not sufficient requirement for the match between models and data because binary mass transfer will result in further dilution and therefore the lowering of the [Rb/Fe] ratios.

¹³C neutron source and therefore the [Rb/Zr] ratio at around solar metallicity to above the values produced by the 3 M_⊙ models. In any case, this is a secondary effect; overall, both these sets of models are comparable to each other and well reproduce the observed spread, except for a few data points with [Rb/Zr] \simeq -1. Since, as described above, lower mass models do not result in lower [Rb/Zr] ratios, to cover such data may require an overall downward shift of the model predictions possibly due to nuclear physics input, such as the rate of the ²²Ne(α ,n)²⁵Mg reaction, which is still very uncertain (Adsley et al. 2020), or the neutron-capture cross sections of the isotopes involved in the branching points.

The other two sets of models included in Fig. 4 cover a smaller metallicity range than the Monash and FRUITY models, but they are still interesting to consider since they produce quite different results, based on different physics. The NuGrid models do not reach

below [Rb/Zr] = -0.45 and are not able to cover the spread of the data. This is due to the overshoot mechanism used in this models at the base of the convective TPs, which results in higher temperature. Our comparison confirms the need, also derived from stardust grain constraints (in particular the ⁹⁶Zr/⁹⁴Zr ratio, see Battino et al. 2019), to somewhat suppress the activation of the ²²Ne in these models. The first SNUPPAT models, based on the ATON stellar evolutionary code, are closer to the NuGrid results, although masses lower than 3 M_⊙ should also be investigated from this set.

Overall, Monash and FRUITY models with mass up to 4 M_⊙ are able to match all the data and models of higher masses, which can reach zero and above for the [Rb/Zr] ratios are not required for the companions of Ba stars. In other words, we have not found in our dataset any Ba stars that could be candidate companions for the IR/OH massive AGB stars with positive [Rb/Zr] ratios reported by

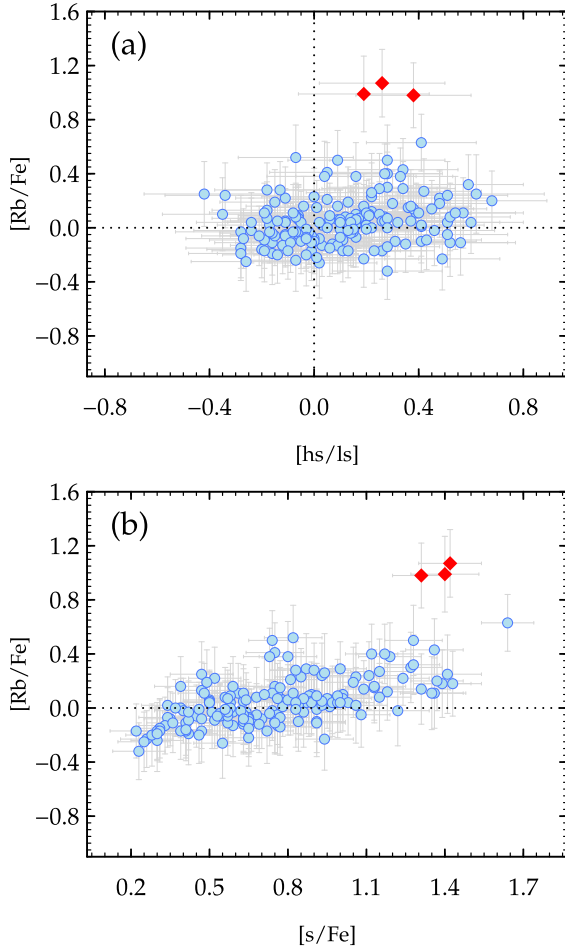


Figure 3. Position of the three most Rb-rich star, HD 120620, BD -09°4337, and MFU 112, in red diamonds, on the planes [Rb/Fe] versus [hs/ls] (panel a) and [Rb/Fe] versus [s/Fe] (panel b).

García-Hernández et al. (2006) and García-Hernández et al. (2009). This may be surprising since according to a simple Salpeter IMF with $\alpha = -2.3$, we expect that out of a stellar population of stars with initial mass 1.5 to 6 M_{\odot} , 14 per cent and 6 per cent should be in the mass range 4 to 6 M_{\odot} or 5 to 6 M_{\odot} , respectively, which corresponds to 25, or 10 stars in our dataset. This difference may point out to some initial mass biases in the production of Ba stars.

8 CONCLUSIONS

To study the *s*-process in AGB stars, we selected a sample consisting of 180 Ba stars and we determined the Rb content in their atmospheres via spectral synthesis of the Rb I line at 7800.2 Å. This element is an efficient diagnostic for the neutron density and therefore points to the neutron source in AGB stars.

The target Ba stars display [Rb/Fe] ranging from -0.4 to $+0.6$ dex, with exception to HD 120620, BD -09°4337, and MFU 112, the three objects more Rb-rich of the sample, with [Rb/Fe] = 1.07, 0.99, and 0.98 dex, respectively. We observed a correlation between the [Rb/Fe] and [Zr/Fe] ratios, showing that Rb production in these stars was not due to activation of the branching points at ^{85}Kr and ^{86}Rb , but rather to an efficient *s*-process inside the AGB companion, because high Rb production is accompanied by high Zr production too. In fact, the anti-correlation observed between the [Rb/Zr] and [Zr/Fe], accompa-

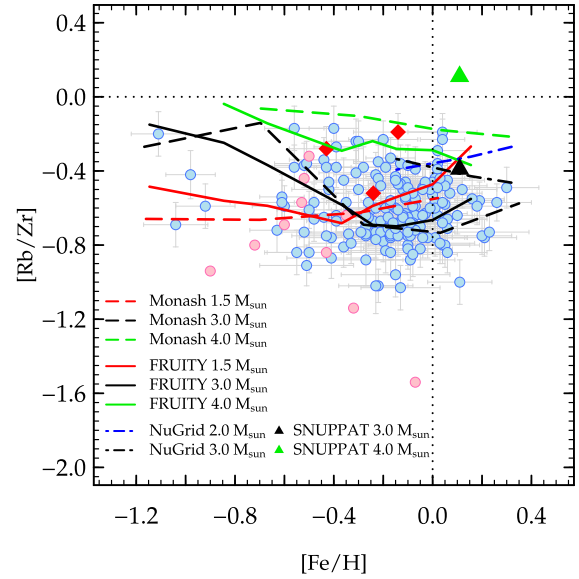


Figure 4. Comparison between observed and theoretical predictions for the [Rb/Zr] ratio. The dot colors have the same meaning of the Fig. 2. The Monash models are from Fishlock et al. (2014), Karakas & Lugaro (2016) and Karakas et al. (2018), the FRUITY models from the FRUITY database (Cristallo et al. 2011), the NuGrid models from Battino et al. (2019), and the SNUPPAT models from Yagüe López et al. (in preparation).

nied by the absence of a trend between [Rb/Zr] and [Rb/Fe] indicate that the spread observed in the dataset is predominantly due to Zr.

We have compared the observed [Rb/Zr] with theoretical predictions from four different sets of available *s*-process models of different masses and metallicities: Monash, FRUITY, NuGrid, and SNUPPAT. Between these models, Monash and FRUITY for low-mass AGB stars were able to match the Rb abundances observed in the atmospheres of the target Ba stars. The observations are consistent with the operation of ^{13}C as main neutron source for the *s*-process in low-mass AGB stars and that the ^{22}Ne source is not efficiently activated in this mass range. Finally, in the present sample, we have not found Ba stars that could be candidates to binary companion for IR/OH massive AGB stars, once the programme stars show [Rb/Zr] < 0.

ACKNOWLEDGEMENTS

We thank the referee for the comments and suggestions. M. P. R. acknowledges financial support by Coordenação de Aperfeiçoamento de Pessoal de Nível Superior (CAPES). M. L. acknowledges the support of the Hungarian National Research, Development and Innovation Office (NKFI), grant KH_18 130405. N. A. D. acknowledges financial support by Russian Foundation for Basic Research (RFBR) according to the research projects 18-02-00554 and 18-52-06004. C. S. thanks the U.S. National Science Foundation for support under grant AST 1616040. C. S. also thanks the Brazilian Astronomical Society and Observatório Nacional for travel support. This work has made use of the VALD database, operated at Uppsala University, the Institute of Astronomy RAS in Moscow, and the University of Vienna.

DATA AVAILABILITY

The data underlying this article will be shared on reasonable request to the corresponding author.

REFERENCES

- Abia C., Wallerstein G., 1998, *MNRAS*, 293, 89
- Abia C., Busso M., Gallino R., Domínguez I., Straniero O., Isern J., 2001, *ApJ*, 559, 1117
- Adsley P. et al., 2020, preprint ([arXiv:2005.14482](https://arxiv.org/abs/2005.14482))
- Allen D. M., Barbuy B., 2006a, *A&A*, 454, 895
- Allen D. M., Barbuy B., 2006b, *A&A*, 454, 917
- Arlandini C., Käppeler F., Wisshak K., Gallino R., Lugaro M., Busso M., Straniero O., 1999, *ApJ*, 525, 886
- Asplund M., Grevesse N., Sauval A. J., 2005, in Barnes Thomas G. I., Bash F. N., eds, ASP Conf. Ser. Vol. 336, Cosmic Abundances as Records of Stellar Evolution and Nucleosynthesis. Astron. Soc. Pac., San Francisco, p. 25
- Asplund M., Grevesse N., Sauval A. J., Scott P., 2009, *ARA&A*, 47, 481
- Battino U. et al., 2016, *ApJ*, 827, 30
- Battino U. et al., 2019, *MNRAS*, 489, 1082
- Bidelman W. P., Keenan P. C., 1951, *ApJ*, 114, 473
- Bize S., Sortais Y., Santos M. S., Mandache C., Clairon A., Salomon C., 1999, *EPL*, 45, 558
- Burris D. L., Pilachowski C. A., Armand roff T. E., Sneden C., Cowan J. J., Roe H., 2000, *ApJ*, 544, 302
- Busso M., Gallino R., Lambert D. L., Travaglio C., Smith V. V., 2001, *ApJ*, 557, 802
- Cowan J. J., Sneden C., Lawler J. E., Aprahamian A., Wiescher M., Langanke K., Martínez-Pinedo G., Thielemann F.-K., 2019, preprint ([arXiv:1901.01410](https://arxiv.org/abs/1901.01410))
- Cristallo S., Straniero O., Gallino R., Piersanti L., Domínguez I., Lederer M. T., 2009, *ApJ*, 696, 797
- Cristallo S. et al., 2011, *ApJS*, 197, 17
- Cristallo S., Straniero O., Piersanti L., Gobrecht D., 2015, *ApJS*, 219, 40
- Cseh B. et al., 2018, *A&A*, 620, A146
- de Castro D. B., Pereira C. B., Roig F., Jilinski E., Drake N. A., Chavero C., Sales Silva J. V., 2016, *MNRAS*, 459, 4299
- Dillmann I., Heil M., Käppeler F., Plag R., Rauscher T., Thielemann F.-K., 2006, KADoNiS- The Karlsruhe Astrophysical Database of Nucleosynthesis in Stars, AIP Conf. Proc. Vol 819, Am. Inst. Phys., New York, p. 123
- D'Orazi V., Lugaro M., Campbell S. W., Bragaglia A., Carretta E., Gratton R. G., Lucatello S., D'Antona F., 2013, *ApJ*, 776, 59
- Escorza A. et al., 2019, *A&A*, 626, A128
- Fishlock C. K., Karakas A. I., Lugaro M., Yong D., 2014, *ApJ*, 797, 44
- Gallino R., Arlandini C., Busso M., Lugaro M., Travaglio C., Straniero O., Chieffi A., Limongi M., 1998, *ApJ*, 497, 388
- García-Hernández D. A., García-Lario P., Plez B., D'Antona F., Manchado A., Trigo-Rodríguez J. M., 2006, *Science*, 314, 1751
- García-Hernández D. A., García-Lario P., Plez B., Manchado A., D'Antona F., Lub J., Habing H., 2007, *A&A*, 462, 711
- García-Hernández D. A. et al., 2009, *ApJ*, 705, L31
- Goriely S., Mowlavi N., 2000, *A&A*, 362, 599
- Grevesse N., Sauval A. J., 1998, *Space Sci. Rev.*, 85, 161
- Grevesse N., Scott P., Asplund M., Sauval A. J., 2015, *A&A*, 573, A27
- Herwig F., 2005, *ARA&A*, 43, 435
- Jorissen A., Boffin H. M. J., Karinkuzhi D., Van Eck S., Escorza A., Shetye S., Van Winckel H., 2019, *A&A*, 626, A127
- Karakas A. I., Lattanzio J. C., 2014, *PASA*, 31, e030
- Karakas A. I., Lugaro M., 2016, *ApJ*, 825, 26
- Karakas A. I., Lugaro M., Carlos M., Cseh B., Kamath D., García-Hernández D. A., 2018, *MNRAS*, 477, 421
- Karinkuzhi D., Goswami A., Sridhar N., Masseron T., Purandardas M., 2018a, *MNRAS*, 476, 3086
- Karinkuzhi D. et al., 2018b, *A&A*, 618, A32
- Katime Santrich O. J., Pereira C. B., de Castro D. B., 2013, *AJ*, 146, 39
- Kaufer A., Stahl O., Tubbesing S., Nørregaard P., Avila G., Francois P., Pasquini L., Pizzella A., 1999, *The Messenger*, 95, 8
- Kervella P., Arenou F., Mignard F., Thévenin F., 2019, *A&A*, 623, A72
- Kurucz R., 1993, CD-ROM No. 13, ATLAS9 Stellar Atmosphere Programs and 2 km/s grid. Smithsonian Astrophysical Observatory, Cambridge
- Käppeler F., Gallino R., Bisterzo S., Aoki W., 2011, *Rev. Modern Phys.*, 83, 157
- Lambert D. L., Smith V. V., Busso M., Gallino R., Straniero O., 1995, *ApJ*, 450, 302
- Lodders K., Palme H., Gail H. P., 2009, *Landolt-Börnstein*, 4B, 712
- Lugaro M., Chieffi A., 2011, in Diehl R., Hartmann D. H., Prantzos N., eds., Lecture Notes in Physics Vol. 112, Radioactivities in Low- and Intermediate-Mass Stars. Springer-Verlag, Berlin, p. 83
- Lugaro M., Herwig F., Lattanzio J. C., Gallino R., Straniero O., 2003, *ApJ*, 586, 1305
- Malaney R. A., 1987, *ApJ*, 321, 832
- Malaney R. A., Lambert D. L., 1988, *MNRAS*, 235, 695
- McClure R. D., 1983, *ApJ*, 268, 264
- McClure R. D., Woodsworth A. W., 1990, *ApJ*, 352, 709
- McClure R. D., Fletcher J. M., Nemec J. M., 1980, *ApJ*, 238, L35
- Mermilliod J. C., Mayor M., 1990, *A&A*, 237, 61
- Mermilliod J. C., Mayor M., Andersen J., Nordstrom B., Lindgren H., Duquennoy A., 1989, *A&AS*, 79, 11
- Morton D. C., 2000, *ApJS*, 130, 403
- Nez F., Biraben F., Felder R., Millerieux Y., 1993, *Optics Commun.*, 102, 432
- Pereira C. B., Drake N. A., 2009, *A&A*, 496, 791
- Pereira C. B., Sales Silva J. V., Chavero C., Roig F., Jilinski E., 2011, *A&A*, 533, A51
- Pignatari M. et al., 2016, *ApJS*, 225, 24
- Piskunov N. E., Kupka F., Ryabchikova T. A., Weiss W. W., Jeffery C. S., 1995, *A&AS*, 112, 525
- Pourbaix D. et al., 2004, *A&A*, 424, 727
- Pérez-Mesa V., Zamora O., García-Hernández D. A., Plez B., Manchado A., Karakas A. I., Lugaro M., 2017, *A&A*, 606, A20
- Rapol U. D., Krishna A., Natarajan V., 2003, *European Phys. J. D*, 23, 185
- Reddy A. B. S., Giridhar S., Lambert D. L., 2013, *MNRAS*, 431, 3338
- Ryabchikova T., Piskunov N., Kurucz R. L., Stempels H. C., Heiter U., Pakhomov Yu., Barklem P. S., 2015, *Phys. Scr.*, 90, 054005
- Sansonetti J. E., 2006, *J. Phys. Chem. Ref. Data*, 35, 301
- Smiljanic R., Porto de Mello G. F., da Silva L., 2007, *A&A*, 468, 679
- Smith V. V., 1984, *A&A*, 132, 326
- Smith V. V., Lambert D. L., 1984, *PASP*, 96, 226
- Sneden C., McWilliam A., Preston G. W., Cowan J. J., Burris D. L., Armosky B. J., 1996, *ApJ*, 467, 819
- Sneden C. A., 1973, PhD thesis, The University of Texas, Austin
- Straniero O., Chieffi A., Limongi M., Busso M., Gallino R., Arlandini C., 1997, *ApJ*, 478, 332
- Tomkin J., Lambert D. L., 1983, *ApJ*, 273, 722
- Tomkin J., Lambert D. L., 1986, *ApJ*, 311, 819
- Tomkin J., Lambert D. L., 1999, *ApJ*, 523, 234
- Travaglio C., Gallino R., Arnone E., Cowan J., Jordan F., Sneden C., 2004, *ApJ*, 601, 864
- Udry S., Jorissen A., Mayor M., Van Eck S., 1998, *A&AS*, 131, 25
- van Raai M. A., Lugaro M., Karakas A. I., García-Hernández D. A., Yong D., 2012, *A&A*, 540, A44
- White H. E., Eliason A. Y., 1933, *Phys. Rev.*, 44, 753
- Woodgate G. K., 1983, *Elementary Atomic Structure*. Oxford Univ. Press, United States
- Ye J., Swartz S., Jungner P., Hall J. L., 1996, *Optics Lett.*, 21, 1280

APPENDIX A

Table A1. Abundance for the whole target Ba stars. First column identifies the objects; columns 2 and 3 give the metallicity and its uncertainty; column 4 gives the logarithmic abundance of Rb; columns 5 and 6 give the [Rb/Fe] ratio and its uncertainty; columns 7 and 8 give the [Zr/Fe] and its uncertainty; columns 9 and 10 display the computed [Rb/Zr] and its uncertainty. Column 11 (Ref.) identifies the source of literature: (1) de Castro et al. (2016); (2) Pereira et al. (2011); (3) Katime Santrich et al. (2013); (4) This work. The last column provides additional information about the binary status of the studied stars. ‘Y’ means ‘yes’ for a binary system, and the number following it indicates the reference for the binary status: (1) Pourbaix et al. (2004); (2) Kervella et al. (2019); (3) Udry et al. (1998); (4) Mermilliod & Mayor (1990); (5) Mermilliod et al. (1989).

Star	[Fe/H]	$\sigma_{\text{[Fe/H]}}$	$\log \epsilon(\text{Rb})$	[Rb/Fe]	$\sigma_{\text{[Rb/Fe]}}$	[Zr/Fe]	$\sigma_{\text{[Zr/Fe]}}$	[Rb/Zr]	$\sigma_{\text{[Rb/Zr]}}$	Ref.	Binarity
BD -08°3194	-0.10	0.16	2.65	+0.15	0.24	+0.95	0.25	-0.80	0.11	1	?
BD -09°4337	-0.24	0.21	3.35	+0.99	0.28	+1.51	0.28	-0.52	0.12	1	?
BD -14°2678	+0.01	0.12	2.70	+0.09	0.21	+0.85	0.20	-0.76	0.10	1	Y1,Y2
CD -27°2233	-0.25	0.18	2.40	+0.05	0.26	+0.73	0.26	-0.68	0.12	1	Y2
CD -29°8822	+0.04	0.15	2.65	+0.01	0.23	+0.81	0.22	-0.80	0.10	1	Y2
CD -30°8774	-0.11	0.14	2.30	-0.19	0.23	+0.27	0.24	-0.46	0.11	1	Y2
CD -38°585	-0.52	0.09	2.30	+0.22	0.20	+0.95	0.21	-0.73	0.11	1	?
CD -42°2048	-0.23	0.16	2.60	+0.23	0.25	+0.96	0.26	-0.73	0.11	1	Y1
CD -53°8144	-0.19	0.15	2.50	+0.09	0.24	+0.80	0.24	-0.71	0.11	1	?
CD -61°1941	-0.20	0.14	2.30	-0.10	0.23	+0.68	0.24	-0.78	0.11	1	Y2
CPD -62°1013	-0.08	0.14	2.60	+0.08	0.22	+0.72	...	-0.64	...	1	?
CPD -64°4333	-0.10	0.18	2.80	+0.30	0.26	+1.12	0.26	-0.82	0.11	1	Y1
HD 4084	-0.42	0.15	2.70	+0.52	0.24	+1.02	0.24	-0.50	0.11	1	Y2
HD 5424	-0.41	0.18	2.30	+0.11	0.26	+0.98	0.26	-0.87	0.11	1	Y1,Y2
HD 5825	-0.48	0.08	2.20	+0.08	0.19	+0.65	0.18	-0.57	0.10	1	Y2
HD 15589	-0.27	0.15	2.60	+0.27	0.24	+1.02	0.24	-0.75	0.11	1	Y2
HD 20394	-0.22	0.12	2.50	+0.12	0.21	+1.14	0.20	-1.02	0.09	1	Y1,Y2
HD 21989	-0.14	0.17	2.20	-0.26	0.26	+0.42	0.27	-0.68	0.11	1	Y2
HD 22285	-0.60	0.13	2.40	+0.40	0.22	+0.99	0.23	-0.59	0.11	1	Y2
HD 22772	-0.17	0.13	2.45	+0.02	0.22	+0.78	0.23	-0.76	0.12	1	Y2
HD 24035	-0.23	0.15	2.55	+0.18	0.24	+1.20	0.25	-1.02	0.15	1	Y1
HD 29370	-0.25	0.16	2.45	+0.10	0.24	+0.71	0.25	-0.61	0.12	1	Y2
HD 29685	-0.07	0.14	2.40	-0.13	0.23	+0.46	0.24	-0.59	0.12	1	Y2
HD 30240	+0.02	0.15	2.55	-0.07	0.23	+0.57	0.22	-0.64	0.10	1	Y2
HD 30554	-0.12	0.14	2.55	+0.07	0.23	+0.57	0.24	-0.50	0.11	1	Y2
HD 32712	-0.24	0.16	2.25	-0.11	0.25	+0.56	0.26	-0.67	0.11	1	Y2
HD 32901	-0.44	0.14	2.05	-0.11	0.24	+0.23	0.25	-0.34	0.12	1	?
HD 35993	-0.05	0.12	2.65	+0.10	0.21	+0.92	0.20	-0.82	0.10	1	Y1,Y2
HD 36650	-0.28	0.13	2.40	+0.08	0.22	+0.46	0.23	-0.38	0.11	1	Y2
HD 38488	+0.05	0.10	2.55	-0.10	0.22	+0.70	0.23	-0.80	0.12	1	Y2
HD 40430	-0.23	0.13	2.35	-0.02	0.22	+0.58	0.23	-0.60	0.12	1	Y2,Y3
HD 43389	-0.50	0.17	2.60	+0.50	0.26	+1.34	0.27	-0.84	0.11	1	Y1,Y2
HD 51959	-0.10	0.15	2.60	+0.10	0.23	+0.76	0.22	-0.66	0.10	1	Y2,Y3
HD 58368	+0.04	0.14	3.05	+0.41	0.22	+0.60	0.21	-0.19	0.10	1	Y1,Y2
HD 59852	-0.22	0.10	2.30	-0.08	0.20	+0.27	0.19	-0.35	0.09	1	Y1,Y2
HD 61332	+0.07	0.13	2.50	-0.17	0.22	+0.35	0.23	-0.52	0.11	1	Y2
HD 64425	+0.06	0.16	2.65	-0.01	0.24	+0.83	0.25	-0.84	0.11	1	?
HD 66291	-0.31	0.15	2.45	+0.16	0.24	+0.57	0.26	-0.41	0.12	1	Y2
HD 67036	-0.41	0.13	2.25	+0.06	0.23	+0.82	0.25	-0.76	0.11	1	?
HD 71458	-0.03	0.10	2.45	-0.12	0.22	+0.51	0.23	-0.63	0.11	1	Y2
HD 74950	-0.21	0.13	2.30	-0.09	0.23	+0.58	0.25	-0.67	0.12	1	Y2
HD 82221	-0.21	0.18	2.45	+0.06	0.26	+0.79	0.28	-0.73	0.12	1	Y2
HD 83548	+0.03	0.14	2.55	-0.08	0.22	+0.71	0.22	-0.79	0.11	1	Y2
HD 84610	+0.00	0.14	2.55	-0.05	0.23	+0.48	0.24	-0.53	0.12	1	Y2
HD 84678	-0.13	0.16	2.65	+0.18	0.25	+1.21	0.26	-1.03	0.12	1	Y1
HD 88035	-0.10	0.18	2.55	+0.05	0.26	+0.80	0.26	-0.75	0.11	1	Y2
HD 88562	-0.27	0.15	2.35	+0.02	0.24	+0.90	0.26	-0.88	0.14	1	Y1,Y2
HD 89175	-0.55	0.13	2.25	+0.20	0.22	+1.04	0.23	-0.84	0.12	1	Y2
HD 91208	+0.05	0.14	2.60	-0.05	0.22	+0.61	0.21	-0.66	0.10	1	Y1,Y2
HD 91979	-0.11	0.12	2.55	+0.06	0.22	+0.69	0.23	-0.63	0.11	1	?
HD 92626	-0.15	0.22	2.70	+0.25	0.29	+1.21	0.29	-0.96	0.12	1	Y1,Y2
HD 105902	-0.18	0.17	2.80	+0.38	0.25	+1.09	0.26	-0.71	0.11	1	?
HD 107264	-0.19	0.17	2.70	+0.29	0.26	+0.89	0.27	-0.60	0.12	1	?
HD 107541	-0.63	0.11	2.60	+0.63	0.21	+1.35	0.20	-0.72	0.12	1	Y1,Y2
HD 110483	-0.04	0.14	2.65	+0.09	0.23	+0.73	0.24	-0.64	0.11	1	?
HD 110591	-0.56	0.12	2.15	+0.11	0.22	+0.28	0.23	-0.17	0.12	1	?
HD 111315	+0.04	0.09	2.70	+0.06	0.20	+0.29	0.21	-0.23	0.11	1	Y2
HD 113291	-0.02	0.16	2.65	+0.07	0.24	+0.83	0.25	-0.76	0.11	1	Y2

Table A1 – continued

Star	[Fe/H]	$\sigma_{\text{[Fe/H]}}$	$\log \epsilon(\text{Rb})$	[Rb/Fe]	$\sigma_{\text{[Rb/Fe]}}$	[Zr/Fe]	$\sigma_{\text{[Zr/Fe]}}$	[Rb/Zr]	$\sigma_{\text{[Rb/Zr]}}$	Ref.	Binarity
HD 116869	-0.36	0.12	2.25	+0.01	0.22	+0.46	0.23	-0.45	0.12	1	Y2
HD 119185	-0.43	0.10	2.00	-0.17	0.21	+0.21	0.22	-0.38	0.12	1	Y2
HD 120571	-0.39	0.09	2.25	+0.04	0.21	+0.31	0.23	-0.27	0.12	1	?
HD 120620	-0.14	0.18	3.53	+1.07	0.25	+1.26	0.24	-0.19	0.10	1	Y1
HD 122687	-0.07	0.13	2.60	+0.07	0.22	+0.71	0.21	-0.64	0.10	1	?
HD 123396	-1.04	0.13	1.60	+0.04	0.23	+0.73	0.25	-0.69	0.12	1	Y2
HD 123701	-0.44	0.09	2.45	+0.29	0.20	+0.94	0.19	-0.65	0.10	1	?
HD 123949	-0.09	0.18	2.65	+0.14	0.26	+1.02	0.28	-0.88	0.11	1	Y1,Y2
HD 126313	-0.10	0.16	2.55	+0.05	0.24	+0.70	0.25	-0.65	0.12	1	Y1
HD 130255	-1.11	0.11	1.65	+0.16	0.22	+0.36	0.24	-0.20	0.12	1	?
HD 131670	-0.04	0.15	2.65	+0.09	0.24	+0.58	0.24	-0.49	0.11	1	Y1,Y2
HD 136636	-0.04	0.18	2.60	+0.04	0.26	+0.80	0.26	-0.76	0.11	1	?
HD 142751	-0.10	0.13	2.45	-0.05	0.23	+0.63	0.25	-0.68	0.11	1	?
HD 143899	-0.27	0.12	2.20	-0.13	0.21	+0.57	0.20	-0.70	0.10	1	Y1,Y2
HD 147884	-0.09	0.15	2.55	+0.04	0.23	+0.79	0.22	-0.75	0.10	1	?
HD 148177	-0.15	0.15	2.50	+0.05	0.24	+0.65	0.26	-0.60	0.11	1	?
HD 154430	-0.36	0.19	2.40	+0.16	0.27	+0.97	0.28	-0.81	0.11	1	Y1
HD 162806	-0.26	0.17	2.40	+0.06	0.26	+0.63	0.27	-0.57	0.12	1	Y2
HD 168214	-0.08	0.10	2.80	+0.28	0.20	+0.96	0.19	-0.68	0.10	1	Y2
HD 168560	-0.13	0.13	2.30	-0.17	0.23	+0.30	0.25	-0.47	0.11	1	Y2
HD 168791	-0.23	0.17	2.75	+0.38	0.26	+0.80	0.27	-0.42	0.12	1	Y2
HD 176105	-0.14	0.12	2.40	-0.06	0.23	+0.41	0.24	-0.47	0.11	1	Y2
HD 177192	-0.17	0.20	2.40	-0.03	0.27	+0.72	0.28	-0.75	0.12	1	?
HD 180996	+0.06	0.15	2.70	+0.04	0.24	+0.49	0.24	-0.45	0.12	1	Y2
HD 182300	+0.06	0.16	2.70	+0.04	0.24	+0.70	0.23	-0.66	0.10	1	?
HD 183915	-0.39	0.14	2.25	+0.04	0.24	+0.68	0.25	-0.64	0.12	1	Y2
HD 187308	-0.08	0.11	2.30	-0.22	0.21	+0.47	0.22	-0.69	0.11	1	Y2
HD 193530	-0.17	0.14	2.40	-0.03	0.24	+0.71	0.25	-0.74	0.12	1	Y2
HD 196445	-0.19	0.17	2.60	+0.19	0.26	+1.02	0.27	-0.83	0.12	1	Y1,Y2
HD 199435	-0.39	0.12	2.35	+0.14	0.21	+0.81	0.20	-0.67	0.09	1	?
HD 200995	-0.03	0.17	2.50	-0.07	0.26	+0.56	0.27	-0.63	0.12	1	Y2
HD 201657	-0.34	0.17	2.50	+0.24	0.25	+0.98	0.26	-0.74	0.11	1	Y1,Y2
HD 201824	-0.33	0.17	2.35	+0.08	0.25	+0.87	0.26	-0.79	0.11	1	Y1,Y2
HD 204075	+0.06	0.17	2.90	+0.24	0.24	+0.95	0.23	-0.71	0.11	1	Y1,Y2
HD 207277	-0.13	0.14	2.30	-0.17	0.24	+0.51	0.25	-0.68	0.12	1	Y2
HD 210709	-0.10	0.14	2.40	-0.10	0.23	+0.39	0.24	-0.49	0.12	1	Y2
HD 210946	-0.12	0.13	2.40	-0.08	0.22	+0.56	0.23	-0.64	0.11	1	Y1,Y2
HD 211173	-0.39	0.09	2.20	-0.01	0.20	+0.37	0.21	-0.38	0.11	1	Y2
HD 211594	-0.43	0.14	2.60	+0.43	0.23	+1.18	0.24	-0.75	0.12	1	Y1,Y2
HD 211954	-0.51	0.19	2.20	+0.11	0.27	+1.02	0.28	-0.91	0.11	1	Y1
HD 214579	-0.26	0.14	2.45	+0.11	0.24	+0.76	0.25	-0.65	0.12	1	Y2
HD 217143	-0.35	0.17	2.30	+0.05	0.26	+0.62	0.27	-0.57	0.12	1	?
HD 217447	-0.17	0.11	2.45	+0.02	0.21	+0.60	0.20	-0.58	0.10	1	Y2
HD 219116	-0.61	0.09	2.10	+0.11	0.20	+0.65	0.21	-0.54	0.12	1	Y2
HD 223586	-0.08	0.11	2.75	+0.23	0.21	+0.82	0.22	-0.59	0.11	1	Y2
HD 223617	-0.18	0.13	2.50	+0.08	0.22	+0.73	0.23	-0.65	0.11	1	Y1,Y2
HD 252117	-0.14	0.19	2.55	+0.09	0.27	+0.84	0.28	-0.75	0.11	1	Y2
HD 273845	-0.15	0.16	2.40	-0.05	0.24	+0.66	0.25	-0.71	0.12	1	?
HD 288174	-0.05	0.15	2.45	-0.10	0.24	+0.60	0.24	-0.70	0.11	1	Y1,Y2
MFU 112	-0.43	0.15	3.15	+0.98	0.24	+1.26	0.24	-0.28	0.12	1	Y1
BD -18°821	-0.27	0.15	2.10	-0.23	0.23	+0.51	0.22	-0.74	0.10	1	?
CD -26°7844	+0.02	0.11	2.75	+0.13	0.21	+0.49	0.20	-0.36	0.10	1	?
CD -30°9005	+0.05	0.12	2.60	-0.05	0.22	+0.53	0.23	-0.58	0.11	1	Y2
CD -34°6139	-0.07	0.13	2.50	-0.03	0.22	+0.69	0.23	-0.72	0.12	1	?
CD -34°7430	+0.01	0.14	2.55	-0.06	0.23	+0.51	0.24	-0.57	0.13	1	?
CD -46°3977	-0.10	0.15	2.40	-0.10	0.24	+0.61	0.24	-0.71	0.11	1	Y2
HD 18182	-0.17	0.10	2.45	+0.02	0.21	+0.35	0.22	-0.33	0.11	1	Y2
HD 18361	+0.01	0.15	2.50	-0.11	0.24	+0.49	0.24	-0.60	0.11	1	Y2
HD 21682	-0.48	0.12	2.00	-0.12	0.21	+0.54	0.20	-0.66	0.12	1	?
HD 26886	-0.30	0.10	2.30	+0.00	0.20	+0.50	0.19	-0.50	0.11	1	Y1,Y2
HD 31812	-0.07	0.11	2.60	+0.07	0.21	+0.62	0.20	-0.55	0.09	1	?
HD 33709	-0.20	0.14	2.40	+0.00	0.22	+0.23	0.21	-0.23	0.10	1	Y2
HD 39778	-0.12	0.12	2.55	+0.07	0.21	+0.72	0.20	-0.65	0.10	1	Y2
HD 41701	+0.02	0.13	2.55	-0.07	0.22	+0.22	0.21	-0.29	0.10	1	Y2

Table A1 – *continued*

Star	[Fe/H]	$\sigma_{\text{[Fe/H]}}$	$\log \epsilon(\text{Rb})$	[Rb/Fe]	$\sigma_{\text{[Rb/Fe]}}$	[Zr/Fe]	$\sigma_{\text{[Zr/Fe]}}$	[Rb/Zr]	$\sigma_{\text{[Rb/Zr]}}$	Ref.	Binarity
HD 45483	−0.14	0.12	2.40	−0.06	0.22	+0.55	0.23	−0.61	0.11	1	Y2
HD 48814	−0.07	0.11	2.40	−0.13	0.21	+0.26	0.22	−0.39	0.12	1	?
HD 49017	+0.02	0.11	2.30	−0.32	0.21	+0.07	0.20	−0.39	0.09	1	?
HD 49661	−0.13	0.10	2.30	−0.17	0.20	+0.19	0.19	−0.36	0.10	1	?
HD 49778	−0.22	0.12	2.15	−0.23	0.21	+0.21	0.20	−0.44	0.10	1	?
HD 50075	−0.16	0.11	2.30	−0.14	0.21	+0.54	0.22	−0.68	0.11	1	?
HD 50843	−0.31	0.13	2.20	−0.09	0.22	+0.15	0.23	−0.24	0.12	1	?
HD 53199	−0.23	0.13	2.30	−0.07	0.22	+0.70	0.21	−0.77	0.11	1	Y1,Y2
HD 58121	−0.01	0.13	2.35	−0.24	0.23	+0.26	0.25	−0.50	0.12	1	Y1,Y2
HD 88495	−0.11	0.10	2.60	+0.11	0.21	+0.66	0.22	−0.55	0.12	1	?
HD 90167	−0.04	0.11	2.40	−0.16	0.21	+0.48	0.20	−0.64	0.12	1	Y2
HD 95193	+0.04	0.12	2.55	−0.09	0.21	+0.48	0.20	−0.57	0.10	1	Y1,Y2
HD 107270	+0.05	0.17	2.90	+0.25	0.24	+0.73	0.23	−0.48	0.11	1	Y2
HD 109061	−0.56	0.09	2.10	+0.06	0.20	+0.44	0.21	−0.38	0.12	1	Y2
HD 113195	−0.15	0.12	2.50	+0.05	0.22	+0.48	0.23	−0.43	0.11	1	?
HD 115277	−0.03	0.15	2.55	−0.02	0.24	+0.45	0.24	−0.47	0.11	1	Y2
HD 119650	−0.10	0.13	2.30	−0.20	0.23	+0.17	0.25	−0.37	0.11	1	Y2
HD 134698	−0.52	0.12	2.30	+0.22	0.23	+0.59	0.24	−0.37	0.12	1	?
HD 139266	−0.27	0.18	2.30	−0.03	0.26	+0.61	0.28	−0.64	0.11	1	?
HD 139409	−0.51	0.13	2.20	+0.11	0.22	+0.47	0.23	−0.36	0.12	1	Y2
HD 169106	+0.01	0.12	2.50	−0.11	0.22	+0.33	0.23	−0.44	0.11	1	Y2
HD 184001	−0.21	0.14	2.55	+0.16	0.22	+0.64	0.21	−0.48	0.10	1	Y2
HD 204886	+0.04	0.15	2.60	−0.04	0.24	+0.64	...	−0.68	...	1	Y2
HD 213084	−0.09	0.15	2.55	+0.04	0.23	+0.72	0.22	−0.68	0.10	1	?
HD 223938	−0.42	0.11	2.25	+0.07	0.21	+0.53	0.20	−0.46	0.10	1	Y2
MFU 214	+0.00	0.12	2.45	−0.15	0.22	+0.31	0.23	−0.46	0.11	1	Y1
MFU 229	−0.01	0.11	2.55	−0.04	0.21	+0.56	0.22	−0.60	0.11	1	?
HD 12392	−0.08	0.18	2.50	−0.02	0.26	+0.83	0.26	−0.85	0.12	1	?
HD 17067	−0.61	0.21	2.25	+0.26	0.29	+0.83	0.30	−0.57	0.12	1	?
HD 90127	−0.40	0.10	2.70	+0.50	0.22	+0.67	0.23	−0.17	0.12	1	Y2
HD 102762	−0.17	0.20	2.45	+0.02	0.28	+0.86	0.29	−0.84	0.12	1	Y2
HD 114678	−0.50	0.13	2.50	+0.40	0.22	+1.01	0.21	−0.61	0.10	1	?
HD 180622	+0.03	0.12	2.60	−0.03	0.23	+0.41	0.24	−0.44	0.12	1	Y1,Y2
HD 200063	−0.34	0.20	2.25	−0.01	0.28	+0.62	0.29	−0.63	0.12	1	Y1,Y2
HD 210030	−0.03	0.11	2.40	−0.17	0.21	+0.29	0.22	−0.46	0.11	1	Y2
HD 214889	−0.17	0.12	2.40	−0.03	0.22	+0.53	0.23	−0.56	0.11	1	?
HD 215555	−0.08	0.12	2.80	+0.28	0.21	+0.80	0.20	−0.52	0.10	1	Y2
HD 216809	−0.04	0.14	2.75	+0.19	0.24	+0.69	0.25	−0.50	0.12	1	?
HD 221879	−0.10	0.19	2.60	+0.10	0.27	+0.83	0.28	−0.73	0.12	1	?
HD 749	−0.29	0.15	2.40	+0.09	0.24	+0.82	0.24	−0.73	0.11	1	Y2
HD 88927	+0.02	0.13	2.45	−0.17	0.23	+0.32	0.25	−0.49	0.12	1	?
BD + 09°2384	−0.98	0.10	2.00	+0.38	0.21	+0.80	0.22	−0.42	0.13	1	?
HD 89638	−0.19	0.11	2.40	−0.01	0.21	+0.37	0.22	−0.38	0.11	1	Y2
HD 187762	−0.30	0.11	2.30	+0.00	0.21	+0.24	0.22	−0.24	0.11	1	Y2
CD −25°6606	+0.12	0.14	2.70	−0.02	0.22	+0.48	0.21	−0.50	0.10	2	?
HD 46040	+0.11	0.13	2.75	+0.04	0.22	+1.04	0.23	−1.00	0.12	2	Y2
HD 49841	+0.21	0.13	2.70	−0.11	0.22	+0.65	0.21	−0.76	0.10	2	Y1,Y2
HD 82765	+0.19	0.10	2.60	−0.19	0.20	+0.37	0.19	−0.56	0.10	2	Y2
HD 84734	+0.20	0.12	2.65	−0.15	0.21	+0.60	0.20	−0.75	0.10	2	?
HD 85205	+0.23	0.16	2.75	−0.08	0.24	+0.65	0.23	−0.73	0.10	2	?
HD 101079	+0.10	0.12	2.50	−0.20	0.21	+0.44	0.20	−0.64	0.10	2	Y3
HD 130386	+0.16	0.13	2.80	+0.04	0.22	+0.59	0.23	−0.55	0.11	2	Y2
HD 139660	+0.26	0.14	2.80	−0.06	0.22	+0.51	0.21	−0.57	0.10	2	Y2
HD 198590	+0.18	0.14	2.70	−0.08	0.22	+0.51	0.21	−0.59	0.10	2	Y2
HD 212209	+0.30	0.13	2.65	−0.25	0.22	+0.24	0.23	−0.49	0.11	2	Y2
NGC 5822-201	−0.11	0.10	2.70	+0.21	0.20	+0.75	0.19	−0.54	0.09	3	Y4
NGC 5822-2	−0.15	0.09	2.60	+0.15	0.20	+0.60	0.19	−0.45	0.10	3	Y1,Y4,Y5
HD 10613	−0.92	0.12	2.00	+0.32	0.22	+0.91	0.23	−0.59	0.12	4	Y2

This paper has been typeset from a \LaTeX file prepared by the author.